iScience

CellPress
OPEN ACCESS

Article

Efficient Construction of a C_{60} Interlayer for Mechanically Robust, Dendrite-free, and Ultrastable Solid-State Batteries

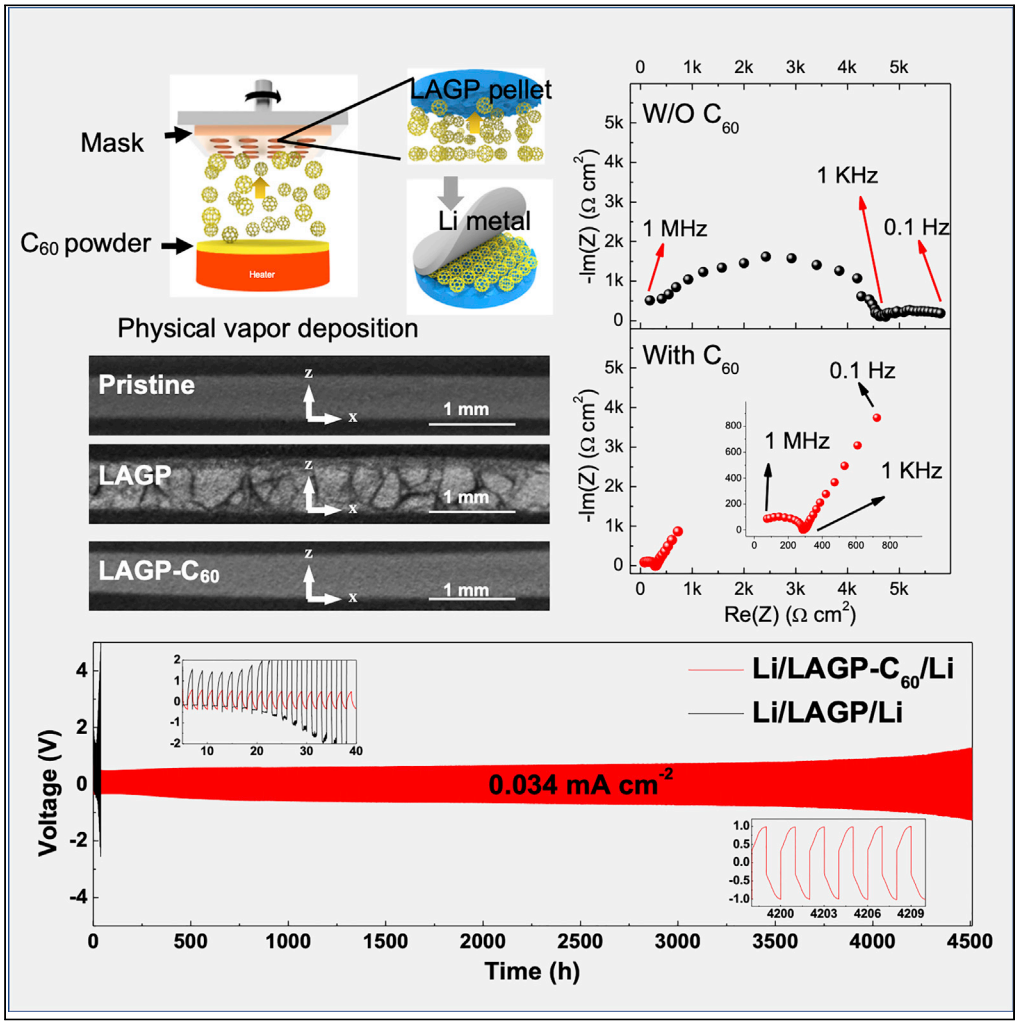

Zhenlong Li, Siwei Zhang, Kun Qian, ..., Tao Li, Guodan Wei, Feiyu Kang

qiankun425@163.com (K.Q.)
weiguodan@sz.tsinghua.edu.cn (G.W.)

HIGHLIGHTS

Ionically conducting Li_xC_{60} matrix is formed at Li-LAGP interface

Li/LAGP-C_{60}/Li cells display ultra-long cycle life of 6 months

Li/LAGP-C_{60}/LFP cells exhibit high capacity with good cycle performance

Mechanical integrity of cycled LAGP-C_{60} is validated by X-ray CT

Li et al., iScience *23*, 101636
October 23, 2020
https://doi.org/10.1016/j.isci.2020.101636

iScience

CellPress
OPEN ACCESS

Article

Efficient Construction of a C_{60} Interlayer for Mechanically Robust, Dendrite-free, and Ultrastable Solid-State Batteries

Zhenlong Li,[1,6] Siwei Zhang,[1,6] Kun Qian,[2,*] Pengbo Nie,[1] Shuxiao Chen,[1] Xuan Zhang,[1] Baohua Li,[3] Tao Li,[2,5] Guodan Wei,[1,7,*] and Feiyu Kang[1,3,4]

SUMMARY

Interfacial instability between solid electrolytes (SEs) and lithium metal remains a daunting challenge for solid-sate batteries. Here, a conformal C_{60} interlayer is efficiently constructed on $Li_{1.5}Al_{0.5}Ge_{1.5}(PO_4)_3$ (LAGP) SEs by physical vapor deposition, and an ideal interfacial contact is achieved via forming an ionically conducting matrix of Li_xC_{60} with lithium metal. The obtained Li_xC_{60} is beneficial to hinder the growth of lithium dendrites at interface and release the local stress during the lithiation and delithiation. As a result, the Li/LAGP-C_{60}/Li symmetric cells demonstrate ultra-stable cycling performance for more than 4,500 h at a current density of 0.034 mA cm^{-2}. The Li/LAGP-C_{60}/$LiFePO_4$ full cells deliver a reversible capacity of 152.4 mAh g^{-1} at room temperature, and the capacity retention rate is 85% after more than 100 cycles. This work provides a feasible and scalable strategy to improve the SEs/Li interface for high-performance solid-state batteries.

INTRODUCTION

Solid electrolytes (SEs) are promising to address the problem of flammability in traditional liquid electrolytes, offering a forward-looking solution for safe and high-energy-density batteries (Bachman et al., 2016; Gao et al., 2018). However, the challenge of cycling failure in solid-state batteries (SSBs) severely restricts their further practical applications, which is predominantly caused by the degradation of solid-solid interfaces (Hao et al., 2019; Luntz et al., 2015). In fact, many studies have shown that lithium dendrites are formed in various types of SEs, such as Na super ion conductor phase (NASICON), e.g., $Li_{1.5}Al_{0.5}Ge_{1.5}(PO_4)_3$ (LAGP) (Hou et al., 2018) and $Li_{1.3}Al_{0.3}Ti_{1.7}(PO_4)_3$ (LATP) (Hao et al., 2019); garnet, e.g., $Li_7La_3Zr_2O_{12}$ (LLZO) (Krauskopf et al., 2019); and Li_2S-P_2S_5 electrolytes (Han et al., 2018; Porz et al., 2017). Even in the very dense garnet-type SEs, the lithium dendrites are able to grow along the grain boundaries and voids (Krauskopf et al., 2019). NASICON-type LAGP SEs have outstanding merits, such as high ionic conductivity (10^{-4}–10^{-3} S cm^{-1}), stability with moisture, and wide electrochemical windows (Feng et al., 2010; Wang et al., 2019). However, the interface degradation is more complicated than garnet, not only because of the formation of dendrites but also because of the poor chemical compatibility caused by Ge^{4+} reduction to Ge^{2+} or even Ge^0 (Hartmann et al., 2013; Lewis et al., 2019). The expendable electronic conducting interphase (MCI) has been observed at Li/SEs interface, which comprises a stoichiometrically changed LAGP and lithium oxide compounds, accompanied by widening microcracks and pulverization, eventually resulting in cell failure (Chung, and Kang, 2017). Tippens et al. (2019) *in situ* observed the growth of the crack network within LAGP during cycling by X-ray computed tomography (CT), which proved that the extent of fracture strongly correlates with increases in impedance.

The interlayer strategy is designed to address these tough interfacial problems in terms of interface protection, interfacial resistance reducing, lithium wettability enhancement, and cycling stability. A typical approach is to introduce an ion-conducting and passivated interlayer between the metallic lithium and SEs, such as polymer-matrix membranes (Zhang et al., 2017), carbon materials (Shao et al., 2018; Feng et al., 2020; Duan et al., 2019), and various types of metal or metal oxide/nitride thin films (Liu et al., 2018a, 2018b; Cheng et al., 2019; Fu et al., 2017), providing good interfacial compatibility via isolating metallic lithium from SEs. Various preparation methods have been developed for functional interlayer materials. For example, solution-based methods were widely used for polymer-matrix interlayers (Peng et al.,

[1]Tsinghua-Berkeley Shenzhen Institute (TBSI), Tsinghua University, Shenzhen 518055, China

[2]Department of Chemistry and Biochemistry, Northern Illinois University, DeKalb, IL 60115, USA

[3]Shenzhen Key Laboratory of Power Battery Safety Research and Shenzhen Geim Graphene Center, Tsinghua Shenzhen International Graduate School, Tsinghua University, Shenzhen 518055, China

[4]School of Materials Science and Engineering, Tsinghua University, Beijing 100084, China

[5]X-ray Science Division, Argonne National Laboratory, Lemont, IL 60439, USA

[6]These authors contributed equally

[7]Lead Contact

*Correspondence: qiankun425@163.com (K.Q.), weiguodan@sz.tsinghua.edu.cn (G.W.)

https://doi.org/10.1016/j.isci.2020.101636

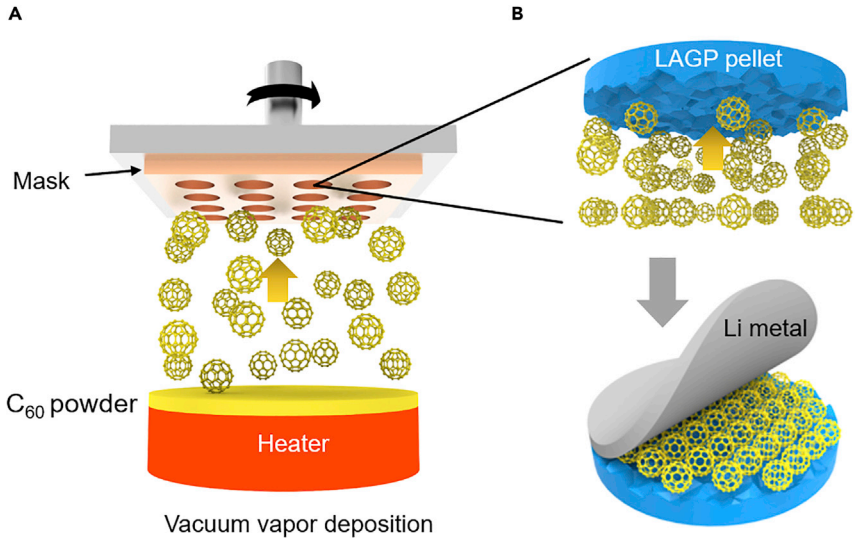

Figure 1. Schematic Diagram of the Construction of C_{60} Interlayer
(A) Schematic diagram of the physical vapor deposition process.
(B) C_{60} interlayer between Li metal anode and SEs.

2017; He et al., 2019; Yu et al., 2019; Liu et al., 2020). Sputtering methods, such as magnetron sputtering and etching sputtering, were employed for metal, metal oxides/nitrides interlayers of ZnO (Hao et al., 2019), Cr (Cortes et al., 2019), Ge (Liu et al., 2018b), Cu_3N (Huo et al., 2020); Polishing methods were reported for removing the surface impurities and simultaneously coating materials, such as MoS_2 (Fu et al., 2019) and Si (Wu et al., 2018); Moreover, nano-structure ZnO (Wang et al., 2017), Al_2O_3 (Han et al., 2017) interlayers were successfully achieved on SEs by atomic layer deposition (ALD) method. However, challenges remain since the current coating methods are either involved in complex multi-step chemical-physical processes or are only applicable to flat SE pellets. Hence, suitable interlayer materials and compatible efficient fabrication technology are still being explored to improve process efficiency and scalability.

Fullerene (C_{60}) is well known for its spheroidal geometry and unique optoelectronic properties and is theoretically electrically insulating but exhibits high electron affinity of 2.65 eV and excellent structure stability (Wang et al., 2012; Haddon, 2002). It can be adopted as a superior SE interlayer material because of its highly reversible electrochemical reaction with metallic lithium and the mechanically soft features to release the compressive stress. More importantly, dense and homogeneous C_{60} layers can be efficiently constructed on SEs surfaces in a controllable manner by one-step physical vapor deposition (PVD). Herein, we have demonstrated that the as-deposited C_{60} molecules can effectively fill the microscopic pores on the LAGP surface to achieve ideal interfacial contact and form ionically conducting matrix of Li_xC_{60}. The obtained Li_xC_{60} exhibits high ionic conductivity but negligible electronic conductivity, which is beneficial to hinder the growth of lithium dendrites at interface and release the local stress during the lithiation and delithiation. As a result, the interfacial impedance of Li-Li symmetric cell is significantly reduced by 15 times. And the cell stably cycles for more than 4,500 h at a current density of 0.034 mA cm^{-2} and over 1,800 h at 0.1 mA cm^{-2}. The Li/LAGP-C_{60}/$LiFePO_4$ cells also obtain a reversible capacity of 152.4 mAh g^{-1} at room temperature with a capacity retention rate of 85% after 100 cycles. By monitoring the mechanical and chemical changes after electrochemical cycling via CT, XPS depth analysis, and SEM, it is found that the C_{60} interlayer successfully suppresses the reduction of Ge^{4+}, the propagation of fracture, and even the formation of dendrites. This work provides a controllable, scalable, and efficient technology to improve the interface stability, hinder the growth of lithium dendrites, and maintain the mechanical integrity of SEs, which may boost the commercial applications of high-performance solid-state batteries.

RESULTS AND DISCUSSION

Figure 1A demonstrates the working process of constructing C_{60} interlayer by physical vapor deposition. The C_{60} power is placed on the evaporator at the bottom of a vacuum chamber, while the SEs were mounted on a top rotating table using a custom-designed mask. The free C_{60} molecules are thermally

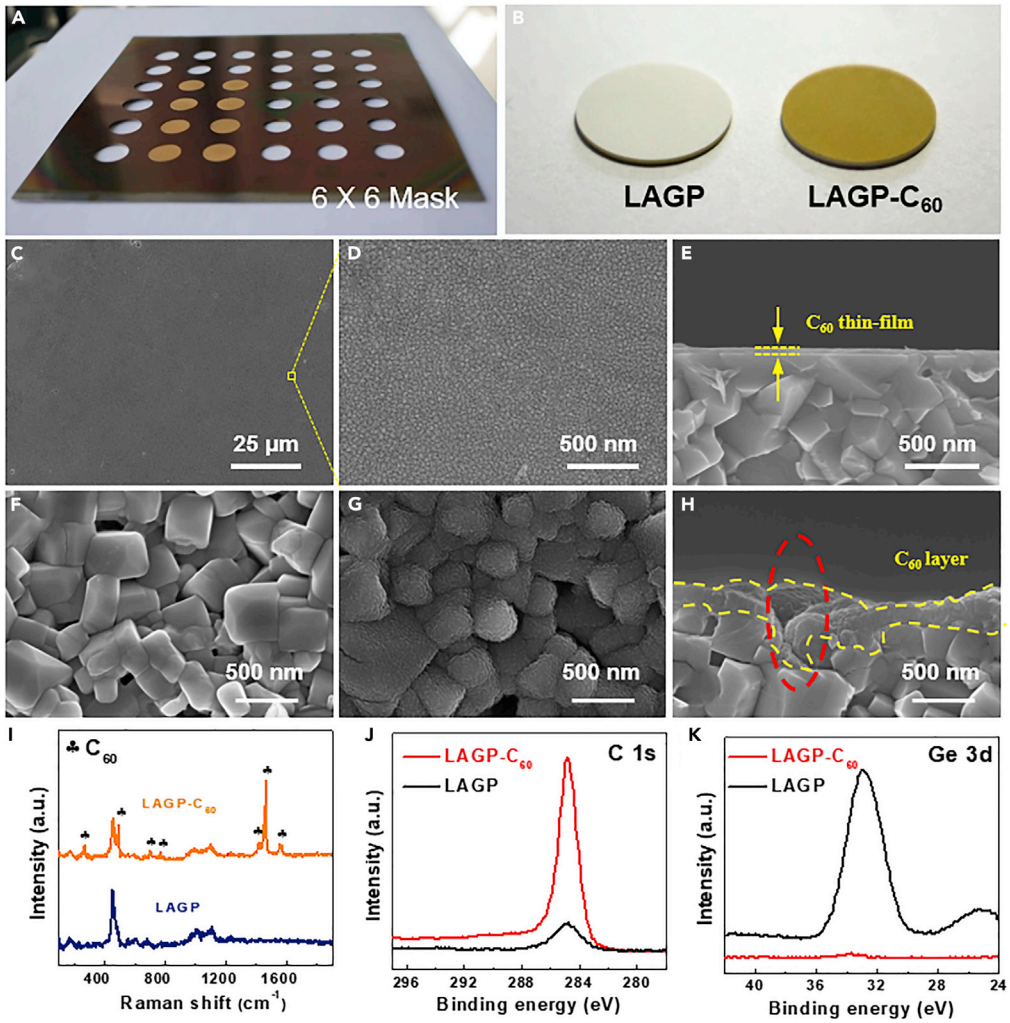

Figure 2. Characterization of Deposited C_{60} Interlayer on LAGP Pellet

(A) Optical image of a 6 × 6 mask for batch deposition.

(B) Optical images of an uncoated LAGP pellet and a coated one in a batch deposition.

(C–E) SEM images of a reference LAGP pellet with C_{60} coating layer; (C) the surface morphology and (D) its partial enlarged view, and (E) its cross-sectional image.

(F–H) SEM images of an unpolished LAGP pellet; (F) the uncoated surface, (G) the coated surface and (H) the cross-sectional image.

(I) Raman spectra of LAGP and LAGP-C_{60}.

(J and K) XPS results of LAGP and LAGP-C_{60}; (J) C 1s spectra and (K) Ge 3d spectra.

evaporated and deposited on the surface of SEs, resulting in a conformal layer of C_{60} thin film in nanoscale (Figure 1B). Notably, the physical vapor deposition method is highly efficient on the interlayer construction and there is no special demanding on the geometries of SEs. In our case, a 6 × 6 mask, as shown in Figure 2A, was employed for batch deposition and 36 LAGP pellets were coated with C60 thin films in 10–15 min. Figure 2B displays optical images of an LAGP pellet before and after batch deposition, in which we can see the color of the surface changed from white to light yellow. A polished reference LAGP pellet was placed with other unpolished LAGP samples for calibrating the actual thickness coating layer. Figures 2C and 2D show the surface morphology of the reference LAGP and its partially enlarged view, respectively. As can be seen, the C_{60} thin films have excellent conformality and uniformity.

In the cross-sectional view (Figure 2E), the thin C_{60} layer can be distinguished and measured by SEM. The unpolished LAGP pellets exhibited very rough surfaces as shown in Figure 2F, which could result in poor

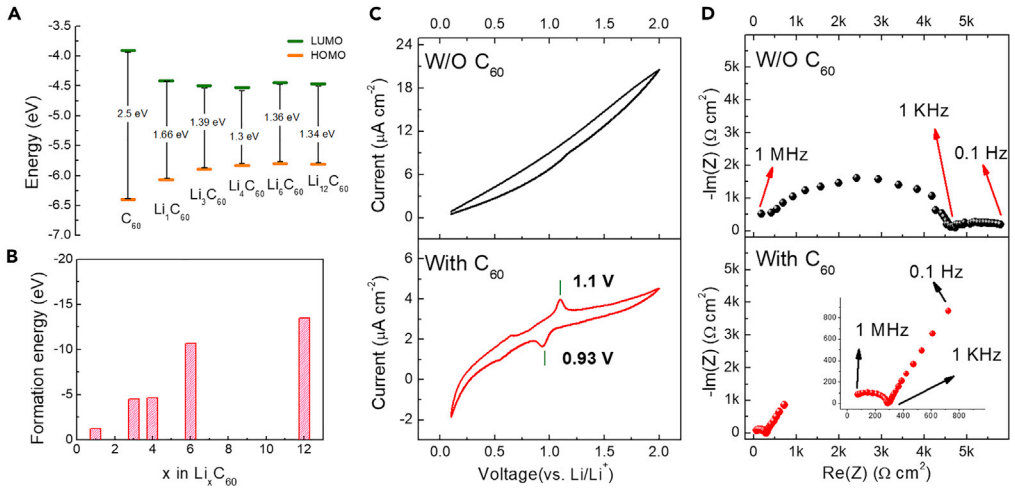

Figure 3. Electrochemical Behavior between Li Metal and C_{60} Interlayer

(A) DFT calculation of energy levels for C_{60} and Li_xC_{60} (x = 1, 3, 4, 6, 12).

(B) DFT calculation of formation energy for Li_xC_{60} (x = 1, 3, 4, 6, 12).

(C) The cyclic voltammetry results of the Li/LAGP/Li and Li/LAGP-C_{60}/Li cells.

(D) The Nyquist plots of the EIS measurements on the Li/LAGP/Li and Li/LAGP-C_{60}/Li cells.

contact after it is assembled with lithium metal anode without interface layer protection. Previous study has proved that polishing the surface can improve the contact and lower down the interfacial resistance (Wang et al., 2018a), but it has inevitably complexed its assembly process since it usually takes extremely time-consuming efforts for preparation, not to mention its inconsistency between pellet to pellet. Herein, the LAGP-C_{60} pellets do not need any further surface treatment, significantly improving their assembly efficiency. Figure 2G shows the SEM image after C_{60} coating; the LAGP surface has a conformal coverage. The C_{60} molecules are able to homogeneously fill the edges and pores of the LAGP layer in Figure 2G, and the rough LAGP surface has been effectively smoothed out from the cross-sectional view in Figure 2H, demonstrating excellent conformal coating of C_{60} film. Raman and XPS spectra of the bare LAGP and LAGP-C_{60} samples are compared in Figures 2I–2K. New Raman bands appeared in the LAGP-C_{60} sample (272, 496, 706, 773, 1,420, 1,466, 1,560 cm^{-1}), which are consistent with previously reported Raman scattering results in C_{60} (Kuzmany et al., 1994). Also, the XPS C1s peak at 284.7 eV increased while the Ge 3d peak disappeared in LAGP-C_{60} sample, which together confirmed that C_{60} layers were constructed and fully covered on LAGP surface.

DFT simulations were carried out to gain a deep understanding of the reaction between C_{60} and lithium metal. Figure 3A displays the electronic structure calculation results for C_{60} and five Li_xC_{60} compounds (x = 1, 3, 4, 6, and 12). The calculated HOMO-LUMO energy gap is 2.5 eV for C_{60}, which is too deep to get free electrons excited effectively, indicating negligible conductivity of pristine C_{60}. In the matrix of Li_xC_{60}, Li ions prefer to locate the octahedral and tetrahedral sites in the gap of densely packed C_{60} molecules (Figure S2). With the injection of Li ions into C_{60} molecules, the calculated LUMO-HOMO gap decreases. Even though the gap values are above 1.3 eV, which indicates that the Li_xC_{60} compounds have better electron transport ability than C_{60}, nevertheless, the electronic conductivity is still very limited. The previous literature indicated that C_{60} can accept up to 12 Li ions and is electrochemically reversible (Allemand et al., 1991; Chabre et al., 1992). Here, we also calculated formation energy of Li with C_{60} as shown in Figure 3B. The negative value of the formation energy means that the chemical reaction is thermodynamically feasible, whereas a larger absolute value represents the reaction is easier to initiate. It can be seen that, as the Li content in Li_xC_{60} increases, the absolute value of formation energy increases, which suggests that Li metal can spontaneously react with C_{60} to form compounds with high lithium content.

Li-Li symmetric cells were assembled to evaluate the electrochemical properties with the introduction of C_{60} layer. Figure 3C compares the cyclic voltammogram of the Li/LAGP/Li and Li/LAGP-C_{60}/Li cells. In the redox cycle for bare LAGP, no reduction peaks were observed. In contrast, for C_{60}-coated LAGP, a pair of well-defined redox peaks appeared at around 1.0 V versus Li/Li^+. The reversible peaks are ascribed

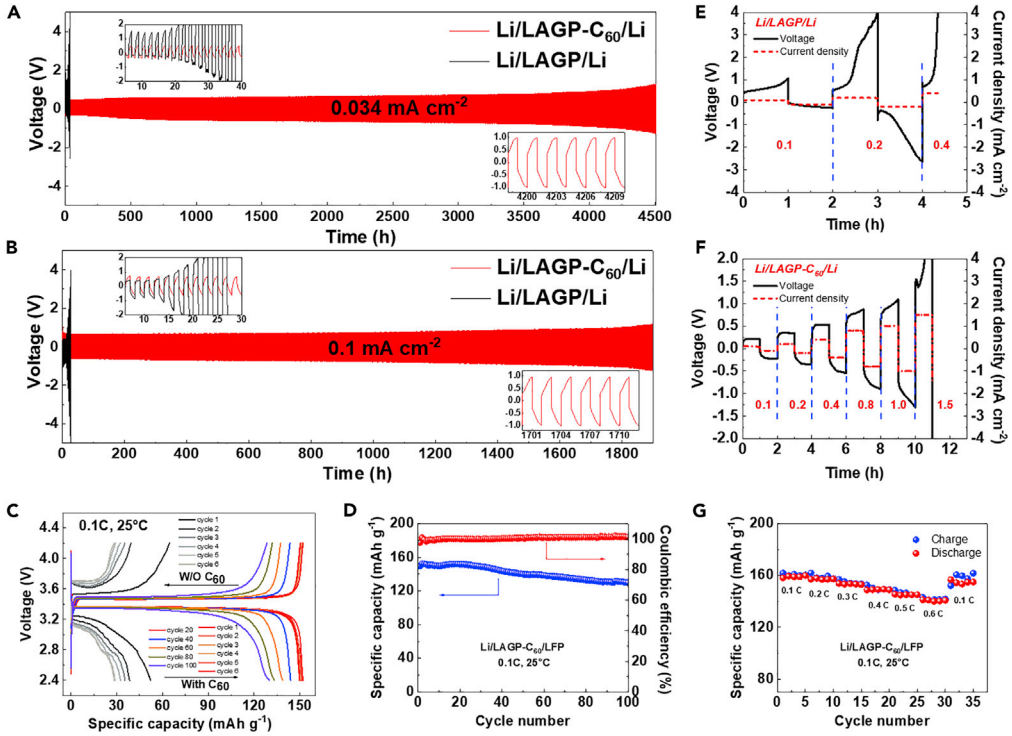

Figure 4. The Electrochemical Performance of Li-Li Symmetric Cells and Li-$LiFePO_4$ Full Cells with and without C_{60} Interlayer

(A and B) Galvanostatic cycling performance of the Li/LAGP/Li and Li/LAGP-C_{60}/Li cells under (A) 0.034 and (B) 0.1 mA cm^{-2}; the insert images are their enlarged view at selected time.

(C) The first six charging and discharging curves of Li/LAGP/$LiFePO_4$ cell and the first six and the 20th, 40th, 60th, 80th, and 100th charging and discharging curves of Li/LAGP-C_{60}/$LiFePO_4$ cell.

(D–F) (D) Cycle performance of Li/LAGP-C_{60}/$LiFePO_4$ cell at 0.1 (C) CCD measurement of Li/LAGP/Li (E) and Li/LAGP-C_{60}/Li (F) symmetric cells.

(G) Rate performance of Li/LAGP-C_{60}/$LiFePO_4$ cell. All the tests were performed at 25°C.

to the insertion reaction of Li_xC_{60}, where x = 4, based on a previous report. (Chabre et al., 1992) The CV results also suggest that the x in Li_xC_{60} is not static but fluctuates with potential during the electrochemical processes, proving the effective Li^+ transport in the interlayer. Therefore, it is Li_xC_{60}, not C_{60}, that played as the actual interlayer, and the actual anode instead of the lithium metal. In the calculated Li_4C_{60} structure, lithium atoms occupied both octahedral and tetrahedral sites (Figure S2). The center-to-center distance between neighboring C_{60} molecules is around 14.1 Å, whereas the calculated C_{60} diameter is 7.1 Å (Stephens et al., 1991; Heiney et al., 1991). Considering such a large space of 7 Å and the radius of lithium ion is only 0.76 Å, the distance of Li and C in Li_xC_{60} is longer than ordinary chemical bonds and thus their interaction is weak, which suggests that the diffusion of Li ions in the C_{60} interlayer is excellent.

The fresh symmetric cells were measured by EIS at 25°C to investigate the impedance change before and after coating. The Nyquist plots of the Li/LAGP/Li and Li/LAGP-C_{60}/Li cells are shown in Figure 3D. In EIS results, the cell impedance includes the bulk impedance, grain boundary impedance, and interface impedance. The bulk resistance is determined from the high-frequency x-intercepts, which are negligible for both cells. A distinct arc was seen in middle-frequency area, which represents the overlap of grain boundary and interface impedances. The cell impedance of Li/LAGP/Li cell is as high as 4,739 Ω cm^{-2}, whereas for the Li/LAGP-C_{60}/Li cell, the cell impedance significantly decreased by 15 times to 290 Ω cm^{-2}. The grain boundary impedance is identical for both cells, which is calculated as 52 Ω cm^{-2} in supporting information (Figure S3). So, the large cell impedance of Li/LAGP/Li cell is mainly originated from the interface impedance, which is likely caused by the poor contact between the rough LAGP surface and lithium metal. C_{60} and its further reaction product of Li_xC_{60} successfully re-constructed the interface and significantly reduced the interface impedance more than one order of magnitude, indicating effectively improved interfacial contact at LAGP-C_{60} cells.

Type of SEs	Layer	Methods	Cycle Time (h)	Current Density (mA cm^{-2})	Temperature	Reference
LAGP	Ge	MS	200	0.3	RT	(Liu et al., 2018b)
LAGP	Cr	MS	850	0.2	RT	(Cortes et al., 2019)
	Cr & Al_2O_3	ALD	1,200	0.2		
LAGP	Polymer		1,100	0.1	60°C	(Zhang et al., 2017)
LATP	ZnO	MS	2,000	0.05	RT	(Hao et al., 2019)
			1,000	0.2	RT	
LATP	Al_2O_3	ALD	600	0.01	RT	(Liu et al., 2018a)
LATP	Polymer	LTCVD	500	0.3	60°C	(Cheng et al., 2019)
LLZO	Al_2O_3	ALD	90	0.2	RT	(Han et al., 2017)
LLZO	Al	EBE	41	0.2	RT	(Fu et al., 2017)
LLZO	Ge	EBE	160	0.05	RT	(Luo et al., 2017)
LLZO	ZnO	ALD	50	0.1	RT	(Wang et al., 2017)
LLZO	Graphite		1,000	0.3	RT	(Shao et al., 2018)
LAGP	C_{60}	PVD	4,500	0.034	RT	This work
			1,800	0.1		

Table 1. Comparison of the Cycling Stability with Different Interlayer Structures

Lithium plating-stripping measurements were carried out by galvanostatic cycling of the symmetric cells at a current density of 0.034 and 0.1 mA cm^{-2}. The charge-discharge voltage profiles of Li/LAGP/Li and Li/LAGP-C_{60}/Li cells are shown in Figure 4A. For the control cell of bare LAGP, the overpotential value increased rapidly upon cycling as shown in the top-left insert image. Only 40 h (20 cycles) of cycling was maintained at the current density of 0.034 mA cm^{-2} and the cycle life was even shorter at a higher current density of 0.1 mA cm^{-2} (top-left insert at Figure 4B). This unstable performance is caused by the continuous and irreversible reaction between LAGP and metallic lithium, which includes the dendrite formation and the reduction of Ge^{4+}.[23] In sharp contrast, the Li/LAGP-C_{60}/Li symmetric cell has demonstrated ultrastable cycling performance, which achieved more than 4,500 h of cycling at 0.034 mA cm^{-2}, whereas the overpotential was still lower than 1 V, as shown by the enlarged voltage profiles, indicating a stable and durable interface with effective lithium ion transport (Figure 4A). Even under a higher current density of 0.1 mA cm^{-2}, 1,800 h of cycling was achieved and the cell maintained a small overpotential (Figure 4B). Table 1 compares the cycling performance of symmetrical cells in this work with previously reported results. As can be seen, our LAGP-C_{60} cells have achieved the longest cycle time so far, which strongly indicates that the Li_xC_{60} interlayer could effectively hinder the growth of lithium dendrites. The critical current density (CCD) of the Li/LAGP/Li and Li/LAGP-C_{60}/Li symmetric cells were tested to study the Li dendrite suppression. Owing to the side reactions of Li metal and LAGP, the interface impedance is dramatically increased under high current, suggesting the rapid degradation of the Li-LAGP interface. As a result, the voltage of Li/LAGP/Li cell increased sharply in 4 h (Figure 4E), resulting in cell failure. In sharp contrast, the cyclic curves of Li/LAGP-C_{60}/Li symmetric cell under different current densities are stable and the critical current density is higher than 1.0 mA cm^{-2} (Figure 4F). These results indicated that the introduction of C_{60} interlayer is conducive to Li dendrite suppression. The previous literature pointed out that the dendrites formation at the interface is caused by the inhomogeneous distribution of electric field, which induces Li nucleation at local position. (Huo et al., 2020) Here, the perfect contacts of Li_xC_{60} with LAGP plus the rapid Li ion migration inside the interlayer has fundamentally reduced chances for Li nucleation and dendrite growth.

To further verify the Li-ion transport capability across the LAGP/Li interface and the interfacial stability, Li/$LiFePO_4$ full cells were assembled and cycled at room temperature. Figure 4C compares the charge-discharge curves of Li/LAGP/$LiFePO_4$ and Li/LAGP-C_{60}/$LiFePO_4$ cells. Although under the same cycling rate of 0.1 C, the charge-discharge plateau gap of Li/LAGP-C_{60}/$LiFePO_4$ cell remains relatively small after

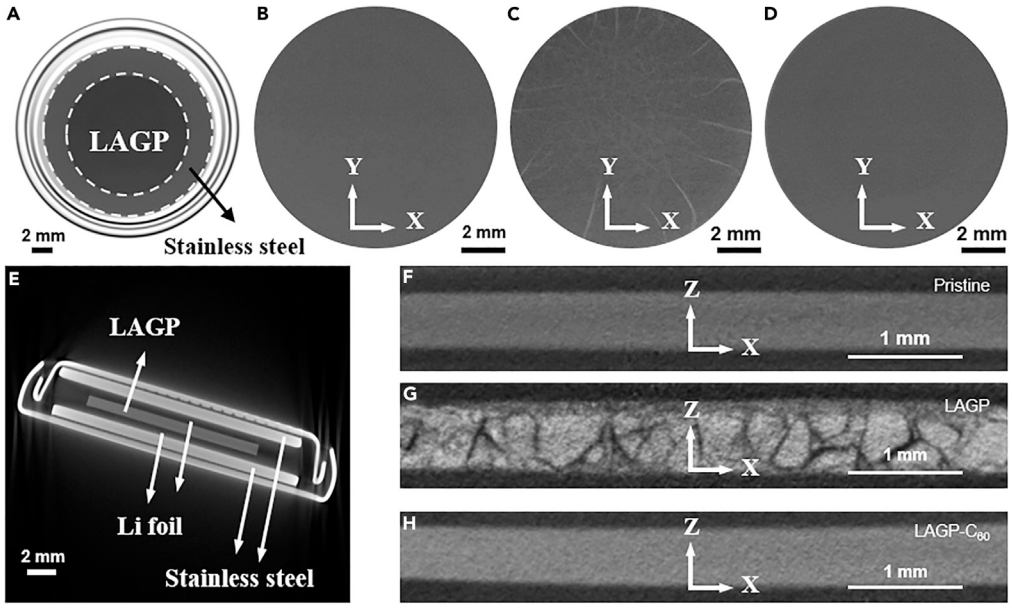

Figure 5. Two-Dimensional X-Ray CT Images of SSBs and LAGP Pellets Extracted from the 3D Tomogram

XY slices of (A) a 2032 type coin cell, (B) pristine LAGP pellet, (C) LAGP pellet after 20 cycles, and (D) LAGP-C_{60} pellet after 150 cycles. XZ slices of (E) the 2032 type coin cell, (F) pristine LAGP pellet, (G) LAGP pellet after 20 cycles, (H) LAGP-C_{60} pellet after 150 cycles.

100 cycles. It is even comparable with the initial cycles of Li/LAGP/$LiFePO_4$ cell, which indicates the small polarization of Li/LAGP-C_{60}/$LiFePO_4$ cell. As shown in Figure 4D, the Li/LAGP-C_{60}/$LiFePO_4$ cell achieved a high initial capacity of 152.4 mAh g^{-1} and a capacity retention rate of 85% after 100 cycles. Therefore, it can be concluded that Li ions are able to effectively transfer from Li_xC_{60} layer to LAGP and finally intercalate into the cathode and vice versa. The coulombic efficiency remains above 98% during 100 cycles, which indicates that the undesired reaction of Li metal and LAGP can be effectively suppressed by introducing a C_{60} layer, thereby achieving good stability of Li/LAGP-C_{60}/$LiFePO_4$ cell. The rate capability of the Li/LAGP-C_{60}/$LiFePO_4$ cell was measured to investigate the cell performance under high current density. The Li/LAGP-C_{60}/$LiFePO_4$ cell delivered specific discharge capacities of 158., 153.9, 145.5, 141.2 mAh g^{-1} at 0.1, 0.3, 0.5, and 0.6 C, respectively (Figure 4G). The cell capacity retention is 97.7% when the current density was adjusted back to 0.1 C, presenting a very stable performance even cycled under high current density. These results suggest that the C_{60} protected LAGP is promising for achieving fast charging in solid-state batteries. X-ray diffraction (XRD) and scanning electron microscope (SEM) measurement were further performed to study the cathodes. There is no obvious change in surface morphology and particle size between the pristine and the cycled $LiFePO_4$ cathodes, whether it is disassembled from the Li/LAGP/$LiFePO_4$ cell or the Li/LAGP-C_{60}/$LiFePO_4$ cell (Figures S5A–S5C). In addition, all the XRD patterns of the pristine and the cycled $LiFePO_4$ cathodes show good structural integrity (Figure S5D). These results indicate that the enhanced battery performance is not contributed by the optimization of the $LiFePO_4$ cathode but by the protection of the Li/LAGP interface.

CT was employed to study the mechanical deformation and internal features of LAGP pellets inside the symmetric cells. CT scanning is able to *ex situ* detect the defects, voids, and cracks without disassembly. The spatial resolution in our experiment is around 2 μm. Figure 5 displays the top view (XY slices) and side view (XZ slices) of a Li/LAGP/Li cell and the extracted SEs from 3D tomogram, the contrast of CT imaging depends on the atomic number, thickness, and density of materials. In Figure 5A, the small internal shadow describes the contour of a LAGP pellet, whereas the large round shadow comes from the stainless steel sheets, which can be easily confirmed in side view (Figure 5E). The lithium metal is invisible in X-ray because of its low atomic number, which explains the gap between solid-state electrolyte and two pieces of stainless steel sheets (Figure 5E). The Li/LAGP/Li and Li/LAGP-C_{60}/Li cells were scanned before and after cycling at 0.034 mA cm^{-2}. Figures 5B–5D displays one horizontal slice from pellets of the pristine LAGP, the cycled LAGP, and the cycled LAGP-C_{60}, respectively, and Figures 5F–5H show their corresponding

side slice images. The pristine LAGP shows a complete structure without internal cracks (Figures 5B and 5F).

Because the CT images for pristine cells with and without C_{60} are similar, only one representative set of images is displayed here. After lithium plating-stripping cycling, we observed crack network formed inside the bare LAGP pellet (Figures 5C and 5G). In side view of Figure 5G, some of the cracks penetrated the entire pellet and others formed a closed loop, reflecting the pulverization of the LAGP after cycling. The crack formation is driven by the stress residual, which is caused by the growth of lithium dendrites and the propagation of MCI. The pulverization of LAGP destroyed the lithium transport channels and well explains the rapid growth of overpotential during lithium plating tests. The LAGP-C_{60} cells have well maintained the mechanical integrality without internal cracks, as shown in Figures 5D and 5H, which is consistent with the ultrastable cycling performance as shown in Figure 4. Apparently, it owes to the protection of Li_xC_{60} interlayer, and its mechanism can be considered as the following three aspects. First, the Li_xC_{60} layer effectively suppressed the reaction of LAGP with metallic lithium, thereby preventing the formation of MCI. Second, the Li_xC_{60} layer eliminated the growth of lithium dendrites at the interface, which hindered the propagation of MCI layer. Third, the softness characteristic of C_{60} and Li_xC_{60} layer is beneficial to alleviate the residual stress and avoid the initiation of cracks and lithium dendrites (Wang et al., 2018b), which is different from the previously reported metal, oxides, or nitrides interlayers that usually have rigid interfacial contact. The mechanical properties of LAGP and LAGP-C_{60} surface were performed by atomic force microscopy (AFM) in peakforce tapping mode to verify the softness of C_{60}. To meet the roughness requirement of AFM testing, the LAGP pellet surface was carefully polished before C_{60} coating and AFM testing. The AFM height maps show the dense and smooth surface of both LAGP (Figure S6A) and LAGP-C_{60} (Figure S6C). The mean Young's modulus of the LAGP surface (Figure S6B) is 1,128 MPa. This value is about 20-fold higher than the mean Young's modulus of the LAGP-C_{60} surface (Figure S6D), which is 57.3 MPa. It proves that the C_{60}-coated surface is very soft, which can release the local stress during the lithiation and delithiation, avoid dendrites and cracks formation, thereby achieving a mechanically robust interface.

The cycled symmetric cells and a fresh control cell were then disassembled in the glove box, and the lithium electrodes were stripped to expose the surfaces of SEs. XPS and SEM characterization were carried out to examine the interfacial chemical states and morphology. All the samples were transferred using an air-tight transfer box to avoid contact and reaction with O_2 or H_2O. Figures 6A and 6B compare the valence change of Ge element in the pristine LAGP, the cycled LAGP, and the cycled LAGP-C_{60}. A sharp peak at 32.9 eV was observed in the XPS Ge 3d spectrum of pristine LAGP, which corresponds to Ge^{4+} (Figure 6A). For cycled LAGP, a new peak appeared at 31.2 eV with low intensity (Figure 6B), which is ascribed to Ge^{2+}, proving that metallic lithium reduced Ge^{4+} to Ge^{2+}. The cycled LAGP-C_{60} shows very weak Ge 3d signal on surface because of the coverage Li_xC_{60} layer. We etched the surface to different depths with Ar^+ beam and collected the Ge 3d spectra every 300 s Figure 6C shows the XPS spectra during 1,800 s of etching. With the removal of the snugly ensconced Li_xC_{60} layer, an increase of Ge 3d peak can be seen with the sputtering time, whereas the corresponding C 1s peak decreases as shown in supporting information (Figure S4). Notably, the peak position of Ge at different depths were consistent, without any offset, suggesting that the valence of Ge keeps at the same state. By fitting the Ge 3d spectrum after 1,800 s of etching, we confirmed the peak position is consistent with that of the pristine LAGP (Figure 6D), proving that the Li_xC_{60} interlayer successfully inhibited the reduction of Ge^{4+}. In addition, no peak position shift was observed in the in-depth C 1s spectra of LAGP-C_{60} (Figure S4), which indicates that the Li_xC_{60} interlayer itself is chemically homogeneous without side reactions.

In the SEM image of cycled LAGP (Figure 6E), we observed lots of reacted black areas, which is discontinuously distributed in the white surface of unreacted LAGP. As a comparison, the surface of cycled LAGP-C_{60} displays a very uniform color (Figure 6F). The section images of SE/Li interface were also collected to investigate the interfacial contact. Owing to the pulverization of uncoated LAGP, many small pieces fell off during sample preparation. In the remaining observable LAGP/Li interface, as shown in Figure 6G, some parts of metallic lithium were found mechanically separated from the LAGP. The cycled Li/LAGP-C_{60} interface still maintained excellent contact, highlighting the bonding functionality of Li_xC_{60} layer (Figure 6H). Figure 6I is the optical images lithium electrodes peeled from LAGP and LAGP-C_{60}. Some pulverized LAGP pieces contaminated lithium surfaces from Li/LAGP sample, whereas a clean lithium surface was observed with C_{60} coating, proving the successful inhibition of side reactions by Li_xC_{60} interlayer. Figures 6J and 6K schematically summarizes the protective mechanism of C_{60} interlayer. For uncoated LAGP, the interface is

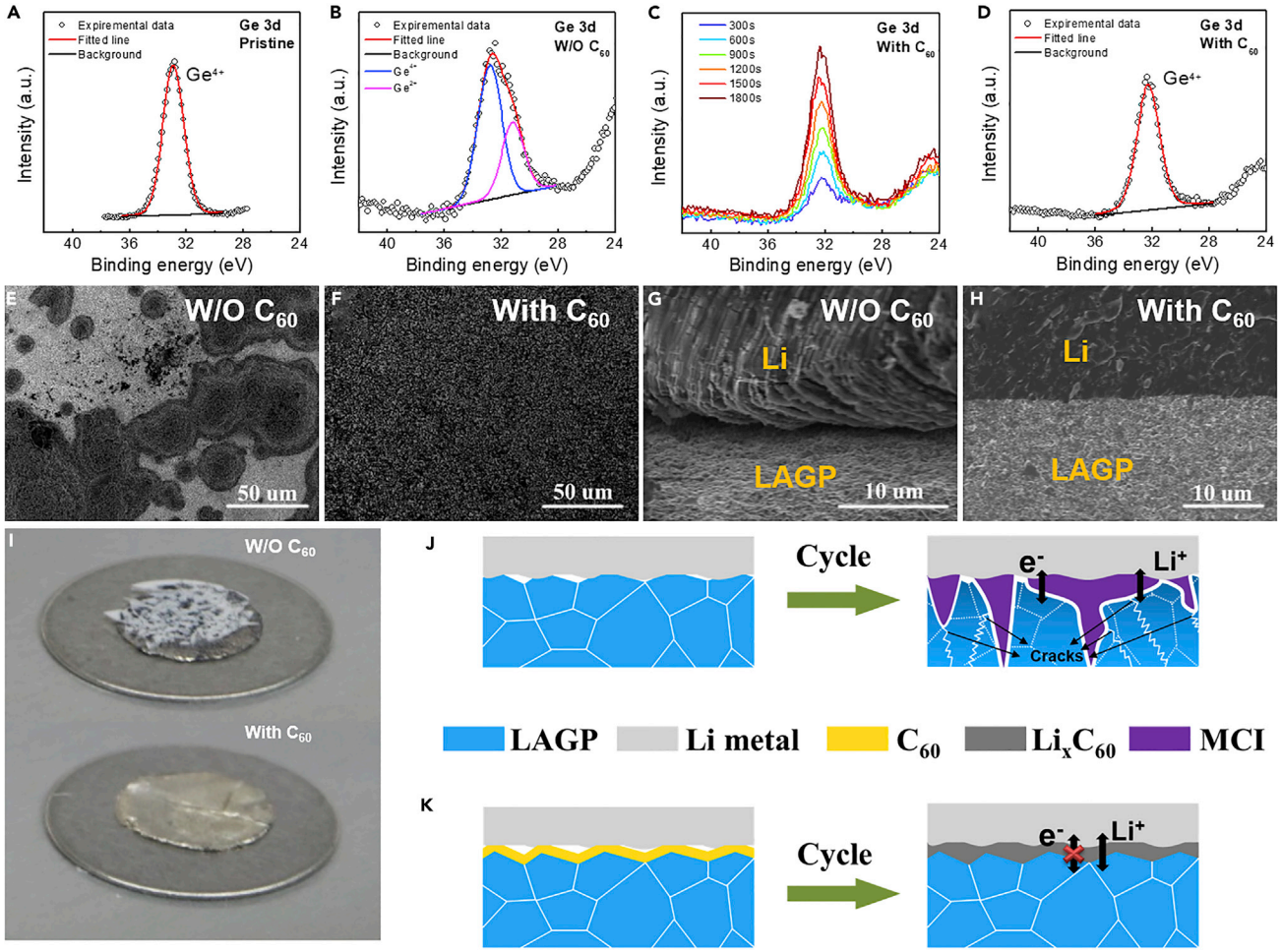

Figure 6. Investigation of Interface Protection Mechanism

XPS spectra of Ge 3d and their fitted results for (A) pristine LAGP and (B) LAGP after 25 cycles. (C) XPS Ge 3d spectra with Ar^+ sputtering at different times for LAGP-C_{60} after 25 cycles. (D) Ge 3d spectra of cycled LAGP-C_{60} after 1 800 s of sputtering and its fitted results. Surface morphology of (E) cycled LAGP and (F) cycled LAGP-C_{60}. Cross-sectional image of (G) cycled Li/LAGP interface and (H) cycled Li/LAGP-C_{60} interface. (I) Optical image of lithium foil surface from cycled Li/LAGP/Li and Li/LAGP-C_{60}/Li cells. The LAGP pellet without C_{60} coating was pulverized after cycling and some white particles adhered to the Li foil. Schematic demonstration of the interface protection mechanism: (J) Li/LAGP interface before and after cycling, (K) Li/LAGP-C_{60} interface before and after cycling.

dominated by a point-to-point reaction owing to the poor contact of LAGP and lithium metal. Owing to the inhomogeneous distribution of electric field, lithium dendrites were induced to grow in local area, which is accompanied by a continuous reaction between metallic lithium and LAGP, and the MCI with black color eventually formed as shown in the Figure 6E. During the cycle, the MCI continuously propagated to the bulk of LAGP owing to its relatively high electronic conductivity. And it caused the pulverization of LAGP pellet and cell impedance skyrocketing. With a C_{60} interlayer, as shown in Figure 6K, the coated C_{60} was first reacted with lithium metal to form a homogeneous Li_xC_{60} layer and re-construct the interface. The close contact made the LAGP/Li_xC_{60} interface dominated by a stable face-to-face reaction, which explains the uniform surface observed by SEM in Figure 6H. Thanks to the improvement on interfacial contact, the cell impedance was reduced by more than one order of magnitude and maintained a low increase after cycling. The tightly wrapped Li_xC_{60} layer successfully isolates the LAGP from metallic lithium, prevents the reduction of Ge^{4+} to Ge^{2+}/Ge^0, and achieves a chemically stable electrode-electrolyte interface. Besides, Li_xC_{60} exhibits high ionic conductivity but negligible electronic conductivity, which is beneficial to hinder the growth of lithium dendrites at the interface. The soft nature of Li_xC_{60} layer can also release the local stress during the lithiation and delithiation, avoiding dendrites and cracks formation, achieving a mechanically robust interface.

Conclusions

Overall, a feasible strategy was proposed to optimize the interface between SEs and metallic lithium in solid state batteries. A conformal C_{60} layer was efficiently built at the Li/SEs interface by PVD. The as-deposited C_{60} can react with lithium to form a stable Li_xC_{60} layer, which has high ionic conductivity but negligible electronic conductivity. This Li_xC_{60} layer effectively suppressed the reduction of LAGP by metallic lithium, significantly improved the interfacial contact, and successfully hindered the growth of lithium dendrites and the propagation of internal cracks. As a result, the assembled Li/LAGP-C_{60}/Li symmetric cell can stably cycle for 4,500 h (more than 6 months) at 0.034 mA cm^{-2} and Li/LAGP-C_{60}/LFP cell can stably cycle for more than 100 times at room temperature. This work provides a controllable and scalable method to improve the SEs/Li interface in one step, which is promising to be applied to other solid electrolyte systems.

Limitations of the Study

There are some limitations to this work. The rate performance of the full battery is limited due to the fact that the intrinsic ionic conductivity of the solid electrolyte used here is much lower than that of the traditional liquid electrolyte. When working at high current density, the transfer of lithium ions in the battery is restricted, which greatly limits the specific capacity and cycle performance of the battery at high current density. Exploring solid electrolyte materials with higher ionic conductivity is an effective method to solve this problem, which requires further research.

Resource Availability

Lead Contact

weiguodan@sz.tsinghua.edu.cn.

Materials Availability

All the materials used in this work are available, and the sourse is stated in the Transparent Method supplemental file.

Data and Code Availability

The data and codes used or analyzed in this work are available from the corresponding authors through reasonable request.

METHODS

All methods can be found in the accompanying Transparent Methods supplemental file.

SUPPLEMENTAL INFORMATION

Supplemental Information can be found online at https://doi.org/10.1016/j.isci.2020.101636.

ACKNOWLEDGMENTS

This research was supported by the National Natural Science Foundation of China (No. 51872157), Shenzhen Municipal Development and Reform Commission, and New Energy Technology Engineering Laboratory (Grant Number: SDRC [2016]172), Shenzhen Technical Plan Project (No. KQJSCX20160226191136, JCYJ20170412170911187, and JCYJ20170817161753629). Z.L. appreciates the help on basic skills from Qi Liu and Aihua Ran in the research.

AUTHOR CONTRIBUTIONS

G.W., K.Q., B.L., and F.K. gave the initial idea of this work. Z.L. and K.Q. performed the experiments and wrote the manuscript. S.Z. contributed to the DFT calculations. P.N. helped draw schematics. S.C., X.Z., and T.L. discussed the results and participated in the preparation of the paper. All authors have given approval to the final version of the manuscript.

DECLARATION OF INTERESTS

There are no conflicts of interest to declare.

Received: July 13, 2020
Revised: August 31, 2020
Accepted: September 28, 2020
Published: October 23, 2020

REFERENCES

Allemand, P.M., Koch, A., Wudl, F., Rubin, Y., Diederich, F., Alvarez, M.M., Anz, S.J., and Whetten, R.L. (1991). Two different fullerenes have the same cyclic voltammetry. J. Am. Chem. Soc. *113*, 1050–1051.

Bachman, J.C., Muy, S., Grimaud, A., Chang, H.H., Pour, N., Lux, S.F., Paschos, O., Maglia, F., Lupart, S., Lamp, P., et al. (2016). Inorganic solid-state electrolytes for lithium batteries: mechanisms and properties governing ion conduction. Chem. Rev. *116*, 140–162.

Chabre, Y., Djurado, D., Armand, M., Romanow, W.R., Coustel, N., McCauley, J.P., Fischer, J.E., and Smith, A.B. (1992). Electrochemical intercalation of lithium into solid fullerene C_{60}. J. Am. Chem. Soc. *114*, 764–766.

Cheng, Q., Li, A., Li, N., Li, S., Zangiabadi, A., Li, T.-D., Huang, W., Li, A.C., Jin, T., Song, Q., et al. (2019). Stabilizing solid electrolyte-anode interface in Li-metal batteries by boron nitride-based nanocomposite coating. Joule *3*, 1510–1522.

Chung, H., and Kang, B. (2017). Mechanical and thermal failure induced by contact between a $Li_{1.5}Al_{0.5}Ge_{1.5}(PO_4)_3$ solid electrolyte and Li metal in an all solid-state Li cell. Chem. Mater. *29*, 8611–8619.

Cortes, F.J.Q., Lewis, J.A., Tippens, J., Marchese, T.S., and McDowell, M.T. (2019). How metallic protection layers extend the lifetime of NASICON-based solid-state lithium batteries. J. Electrochem. Soc. *167*, 050502.

Duan, J., Wu, W., Nolan, A.M., Wang, T., Wen, J., Hu, C., Mo, Y., Luo, W., and Huang, Y. (2019). lithium–graphite paste: an interface compatible anode for solid-state batteries. Adv. Mater. *31*, 1807243.

Feng, J.K., Lu, L., and Lai, M.O. (2010). Lithium storage capability of lithium ion conductor $Li_{1.5}Al_{0.5}Ge_{1.5}(PO_4)_3$. J. Alloys Compd. *501*, 255–258.

Feng, W., Dong, X., Zhang, X., Lai, Z., Li, P., Wang, C., Wang, Y., and Xia, Y. (2020). Li/garnet interface stabilization by thermal-decomposition vapor deposition of an amorphous carbon layer. Angew. Chem. Int. Ed. *59*, 5346–5349.

Fu, K.K., Gong, Y., Liu, B., Zhu, Y., Xu, S., Yao, Y., Luo, W., Wang, C., Lacey, S.D., Dai, J., et al. (2017). Toward garnet electrolyte-based Li metal batteries: an ultrathin, highly effective, artificial solid-state electrolyte/metallic Li interface. Sci. Adv. *3*, e1601659.

Fu, J., Yu, P., Zhang, N., Ren, G., Zheng, S., Huang, W., Long, X., Li, H., and Liu, X. (2019). In situ formation of a bifunctional interlayer enabled by a conversion reaction to initiatively prevent lithium dendrites in a garnet solid electrolyte. Energy Environ. Sci. *12*, 1404–1412.

Gao, Z., Sun, H., Fu, L., Ye, F., Zhang, Y., Luo, W., and Huang, Y. (2018). Promises, challenges, and recent progress of inorganic solid-state electrolytes for all-solid-state lithium batteries. Adv. Mater. *30*, e1705702.

Haddon, R.C. (2002). Electronic structure, conductivity and superconductivity of alkali metal doped (C_{60}). Acc. Chem. Res. *25*, 127–133.

Han, X., Gong, Y., Fu, K.K., He, X., Hitz, G.T., Dai, J., Pearse, A., Liu, B., Wang, H., Rubloff, G., et al. (2017). Negating interfacial impedance in garnet-based solid-state Li metal batteries. Nat. Mater. *16*, 572–579.

Han, F.D., Yue, J., Zhu, X.Y., and Wang, C.S. (2018). Suppressing Li dendrite formation in Li_2S-P_2S_5 solid electrolyte by LiI incorporation. Adv. Energy Mater. *8*, 1703644.

Hao, X., Zhao, Q., Su, S., Zhang, S., Ma, J., Shen, L., Yu, Q., Zhao, L., Liu, Y., Kang, F., et al. (2019). Constructing multifunctional interphase between $Li_{1.4}Al_{0.4}Ti_{1.6}(PO_4)_3$ and Li metal by magnetron sputtering for highly stable solid-state lithium metal batteries. Adv. Energy Mater. *9*, 1901604.

Hartmann, P., Leichtweiss, T., Busche, M.R., Schneider, M., Reich, M., Sann, J., Adelhelm, P., and Janek, J. (2013). Degradation of NASICON-type materials in contact with lithium metal: formation of mixed conducting interphases (MCI) on solid electrolytes. J. Phys. Chem. C *117*, 21064–21074.

He, L., Sun, Q., Chen, C., Oh, J.A.S., Sun, J., Li, M., Tu, W., Zhou, H., Zeng, K., and Lu, L. (2019). Failure mechanism and interface engineering for NASICON-structured all-solid-state lithium metal batteries. ACS Appl. Mater. Interfaces *11*, 20895–20904.

Heiney, P.A., Fischer, J.E., McGhie, A.R., Romanow, W.J., Denenstein, A.M., McCauley, J.P., Jr., Smith, A.B., and Cox, D.E. (1991). Orientational ordering transition in solid C_{60}. Phys. Rev. Lett. *66*, 2911–2914.

Hou, G.M., Ma, X.X., Sun, Q.D., Ai, Q., Xu, X.Y., Chen, L.N., Li, D.P., Chen, J.H., Zhong, H., Li, Y., et al. (2018). Lithium dendrite suppression and enhanced interfacial compatibility enabled by an ex situ SEI on Li anode for LAGP-based all-solid-state batteries. ACS Appl. Mater. Interfaces *10*, 18610–18618.

Huo, H., Chen, Y., Li, R., Zhao, N., Luo, J., Pereira da Silva, J.G., Mücke, R., Kaghazchi, P., Guo, X., and Sun, X. (2020). Design of a mixed conductive garnet/Li interface for dendrite-free solid lithium metal batteries. Energy Environ. Sci. *13*, 127–134.

Krauskopf, T., Dippel, R., Hartmann, H., Peppler, K., Mogwitz, B., Richter, F.H., Zeier, W.G., and Janek, J. (2019). Lithium-metal growth kinetics on LLZO garnet-type solid electrolytes. Joule *3*, 2030–2049.

Kuzmany, H., Matus, M., Burger, B., and Winter, J. (1994). Raman scattering in C_{60} fullerenes and fullerides. Adv. Mater. *6*, 731–745.

Lewis, J.A., Cortes, F.J.Q., Boebinger, M.G., Tippens, J., Marchese, T.S., Kondekar, N., Liu, X.M., Chi, M.F., and McDowell, M.T. (2019). Interphase morphology between a solid-state electrolyte and lithium controls cell failure. ACS Energy Lett. *4*, 591–599.

Liu, Y., Sun, Q., Zhao, Y., Wang, B., Kaghazchi, P., Adair, K.R., Li, R., Zhang, C., Liu, J., Kuo, L.Y., et al. (2018a). Stabilizing the interface of NASICON solid electrolyte against Li metal with atomic layer deposition. ACS Appl. Mater. Interfaces *10*, 31240–31248.

Liu, Y., Li, C., Li, B., Song, H., Cheng, Z., Chen, M., He, P., and Zhou, H. (2018b). Germanium thin film protected lithium aluminum germanium phosphate for solid-state Li batteries. Adv. Energy Mater. *8*, 1702374.

Liu, Q., Yu, Q.P., Li, S., Wang, S.W., Zhang, L.H., Cai, B.Y., Zhou, D., and Li, B.H. (2020). Safe LAGP-based all solid-state Li metal batteries with plastic super-conductive interlayer enabled by in-situ solidification. Energy Storage Mater. *25*, 613–620.

Luntz, A.C., Voss, J., and Reuter, K. (2015). Interfacial challenges in solid-state Li ion batteries. J. Phys. Chem. Lett. *6*, 4599–4604.

Luo, W., Gong, Y., Zhu, Y., Li, Y., Yao, Y., Zhang, Y., Fu, K., Pastel, G., Lin, C.F., and Mo, Y. (2017). Reducing interfacial resistance between garnet-structured solid-state electrolyte and Li-metal anode by a germanium layer. Adv. Mater. *29*, 1606042.

Peng, Z., Zhao, N., Zhang, Z., Wan, H., Lin, H., Liu, M., Shen, C., He, H., Guo, X., Zhang, J.-G., et al. (2017). Stabilizing Li/electrolyte interface with a transplantable protective layer based on nanoscale LiF domains. Nano Energy *39*, 662–672.

Porz, L., Swamy, T., Sheldon, B.W., Rettenwander, D., Fromling, T., Thaman, H.L., Berendts, S., Uecker, R., Carter, W.C., and Chiang, Y.M. (2017). Mechanism of lithium metal penetration through inorganic solid electrolytes. Adv. Energy Mater. *7*, 1701003.

Shao, Y., Wang, H., Gong, Z., Wang, D., Zheng, B., Zhu, J., Lu, Y., Hu, Y.-S., Guo, X., Li, H., et al. (2018). Drawing a soft interface: an effective interfacial modification strategy for garnet-type solid-state Li batteries. ACS Energy Lett. *3*, 1212–1218.

Stephens, P.W., Mihaly, L., Lee, P.L., Whetten, R.L., Huang, S.-M., Kaner, R., Deiderich, F., and Holczer, K. (1991). Structure of single-phase superconducting K3C60. Nature *351*, 632–634.

Tippens, J., Miers, J.C., Afshar, A., Lewis, J.A., Cortes, F.J.Q., Qiao, H., Marchese, T.S., Di Leo,

C.V., Saldana, C., and McDowell, M.T. (2019). Visualizing chemomechanical degradation of a solid-state battery electrolyte. ACS Energy Lett. *4*, 1475–1483.

Wang, H., He, Y., Li, Y., and Su, H. (2012). Photophysical and electronic properties of five PCBM-like C60 derivatives: spectral and quantum chemical view. J. Phys. Chem. A *116*, 255–262.

Wang, C., Gong, Y., Liu, B., Fu, K., Yao, Y., Hitz, E., Li, Y., Dai, J., Xu, S., Luo, W., et al. (2017). Conformal, nanoscale ZnO surface modification of garnet-based solid-state electrolyte for lithium metal anodes. Nano Lett. *17*, 565–571.

Wang, S., Wang, J., Liu, J., Song, H., Liu, Y., Wang, P., He, P., Xu, J., and Zhou, H. (2018a). Ultra-fine surface solid-state electrolytes for long cycle life all-solid-state lithium–air batteries. J. Mater. Chem. C *6*, 21248–21254.

Wang, X., Zeng, W., Hong, L., Xu, W., Yang, H., Wang, F., Duan, H., Tang, M., and Jiang, H. (2018b). Stress-driven lithium dendrite growth mechanism and dendrite mitigation by electroplating on soft substrates. Nat. Energy *3*, 227.

Wang, L., Hu, S., Su, J., Huang, T., and Yu, A. (2019). Self-sacrificed interface-based on the flexible composite electrolyte for high-performance all-solid-state lithium batteries. ACS Appl. Mater. Interfaces *11*, 42715–42721.

Wu, B.B., Wang, S.Y., Lochala, J., Desrochers, D., Liu, B., Zhang, W.Q., Yang, J.H., and Xiao, J. (2018). The role of the solid electrolyte interphase layer in preventing Li dendrite growth in solid-state batteries. Energy Environ. Sci. *11*, 1803–1810.

Yu, Q., Han, D., Lu, Q., He, Y.B., Li, S., Liu, Q., Han, C., Kang, F., and Li, B. (2019). Constructing effective interfaces for $Li_{1.5}Al_{0.5}Ge_{1.5}(PO_4)_3$ pellets to achieve room-temperature hybrid solid-state lithium metal batteries. ACS Appl. Mater. Interfaces *11*, 9911–9918.

Zhang, Z., Zhao, Y., Chen, S., Xie, D., Yao, X., Cui, P., and Xu, X. (2017). An advanced construction strategy of all-solid-state lithium batteries with excellent interfacial compatibility and ultralong cycle life. J. Mater. Chem. C *5*, 16984–16993.

iScience, Volume *23*

Supplemental Information

Efficient Construction of a C_{60} Interlayer for Mechanically Robust, Dendrite-free, and Ultrastable Solid-State Batteries

Zhenlong Li, Siwei Zhang, Kun Qian, Pengbo Nie, Shuxiao Chen, Xuan Zhang, Baohua Li, Tao Li, Guodan Wei, and Feiyu Kang

Transparent Methods

LAGP pellet preparation.

The LAGP powder (Hefei Kejing materials technology Co., China) was compacted into a circular mold (diameter:13 mm) at a pressure of 2 MPa, and then sintered at 850 ℃ for 12 hours to obtain LAGP pellets with a diameter of around 11 mm and a thickness of about 750 μm.

C_{60} coating by physical vapor deposition.

The C_{60} powder was purchased from Shanghai Macklin Biochemical Technology Co., China. The C_{60} interlayer was constructed by physical vapor deposition on LAGP surfaces with a home-designed 6×6 mask. In the deposition process, the vacuum of the chamber was below 6×10^{-4} Pa. The deposition rate is ranged from 0.05 Å s^{-1} to 0.3 Å s^{-1}. The LAGP were coated on one side or both sides for Li/LAGP-C_{60}/$LiFePO_4$ cells and Li/LAGP-C_{60}/Li symmetric cells, respectively.

Cell assembly and testing.

2032-type coin cells were assembled inside an argon filled glovebox. Li pellets were put onto two sides of the LAGP and LAGP-C_{60} pellet and then sealed to obtain Li/LAGP/Li and Li/LAGP-C_{60}/Li symmetric cells, respectively. An elastic conductive layer was used instead of steel shrapnel to avoid the crack of brittle SEs during sealing. The full cells were also assembled in the glovebox. The $LiFePO_4$ cathode was prepared by mixing the $LiFePO_4$ powder, Super P, and polyvinylidene fluoride (PVDF) in N-methyl pyrrolidone (NMP), and then coated on an Al foil with a loading mass of ~2.0 mg cm^{-2}. 5 uL liquid electrolyte composed of 1 M lithium hexafluorophosphate ($LiPF_6$) in the mixture of ethylene carbonate (EC), diethyl carbonate (DEC) and dimethyl carbonate (DMC) (volume ratio: 1:1:1) was added between the $LiFePO_4$ cathode and the LAGP SE in Li/LAGP/$LiFePO_4$ and Li/LAGP-C_{60}/$LiFePO_4$ cells. All the electrochemical tests were carried out at room temperature using a Land 2001A battery testing system. The symmetric cells were charged and discharged for 2 h each charge and discharge. The upper and lower cut-off voltages of $LiFePO_4$ full cells were 4.2 V and 2.4 V, respectively. The cycling rate was 0.1 C and the theoretical capacity of $LiFePO_4$ was set as 170 mAh g^{-1}. Electrochemical impedance spectroscopy (EIS) and cyclic voltammetry (CV) tests were carried out on the SP-300 electrochemical station. Impedance tests were applied with a frequency range of 100 mHz to 7 MHz and an amplitude of 10 mV. The applied CV scan rate is 0.2 mV s^{-1}.

Material characterization.

The X-ray diffraction (XRD) patterns were performed using a Bruker D8 Advance X-ray Diffractometer using Cu Kα radiation (λ = 0.154 nm). The XRD tests operated at 40 kV and 40 mA with a step size of 0.02° (2θ from 10° to 80° with 5° min^{-1}). The LAGP powder and pellet samples have a perfect crystal structure of $LiGe_2(PO_4)_3$ (Figure S1). The Raman spectra were obtained by Horiba LabRAM HR800 with a laser of 532nm. The X-ray photoelectron spectra (XPS) spectra were performed in a PHI 5000 VersaProbe II spectrometer using an Al Kα monochromatization of radiation (hν = 1486.6 eV) beam (100 μm, 25 W, 15 kV). All binding energies were referenced to the C 1s peak at 284.8 eV of the surface adventitious carbon to correct the shift caused by charge effect. XPS depth profiling were carried out by etching the sample by Ar^+ ion beam. The Ge 3d spectra were collected after 300 s, 600 s, 900 s, 1200 s, 1500 s, and 1800 s of etching, respectively. Morphological characterization was performed by using a Hitachi SU-8010 scanning electron microscope (SEM). The sample for cross-section SEM investigation were prepared by breaking the LAGP (LAGP-C_{60}) pellets or the LAGP (LAGP-C_{60})/Li metal using a diagonal pliers. Samples for SEM and XPS characterization were prepared in a glove box with Ar atmosphere and transferred in an air-tight transfer box. X-ray computed tomography was performed using Werth TomoScope L 300 from Werth Messtechnik GmbH. The applied voltage and current were 160 kV and 280 uA, respectively. The projection images were all acquired over an exposure time of 500 ms. A Cu filter with a thickness of 0.2 mm was used to avoid overexposure. The spatial resolution was 2 μm. The mechanical properties of LAGP and LAGP-C_{60} surface were performed by Atomic Force Microscopy (AFM) (Bruker Dimension Ico) in peakforce tapping mode. The RTESPA-525 probe and RTESPA-300 probe were used for the AFM testing of LAGP and LAGP-C_{60}, respectively. The polystyrene standard sample was used for calibration.

Density functional theory (DFT) simulations.

DFT calculations were performed in Gaussian 16 using the B3LYP exchange-correlation functionals and 6-31+g (d,p) basis set. Tight convergence criteria were used for structure optimization. The energy of one free Li atom (E_{Li}) was estimated by $E_{Li} = E_{atom/bcc} - E_{coh}$, where the $E_{atom/bcc}$ is the energy of a Li atom in a *bcc* (body-centered cubic) structure and E_{coh} stands for the cohesive energy of *bcc* Li taken as 1.63 eV $atom^{-1}$. The formation energies E_f of Li_xC_{60} were computed as $E_f = E_{Li_xC_{60}} - E_{C_{60}} - xE_{Li}$, where $E_{Li_xC_{60}}$ and $E_{C_{60}}$ is the

energy of Li_xC_{60} and C_{60}, respectively. The voltage ($V_{Li_xC_{60}}$) of lithium intercalation C_{60} was estimated by $V_{Li_xC_{60}} = \frac{E_f}{xe}$, e is the electrical charge.

Supplemental Figures

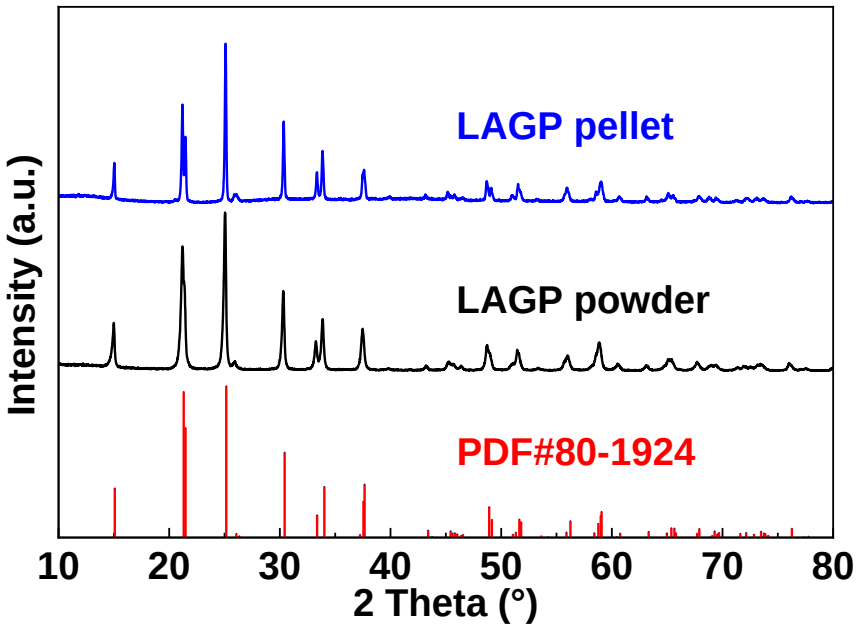

Figure. S1 XRD pattern of LAGP powder and sintered LAGP pellet. **Related to Figure 2.**

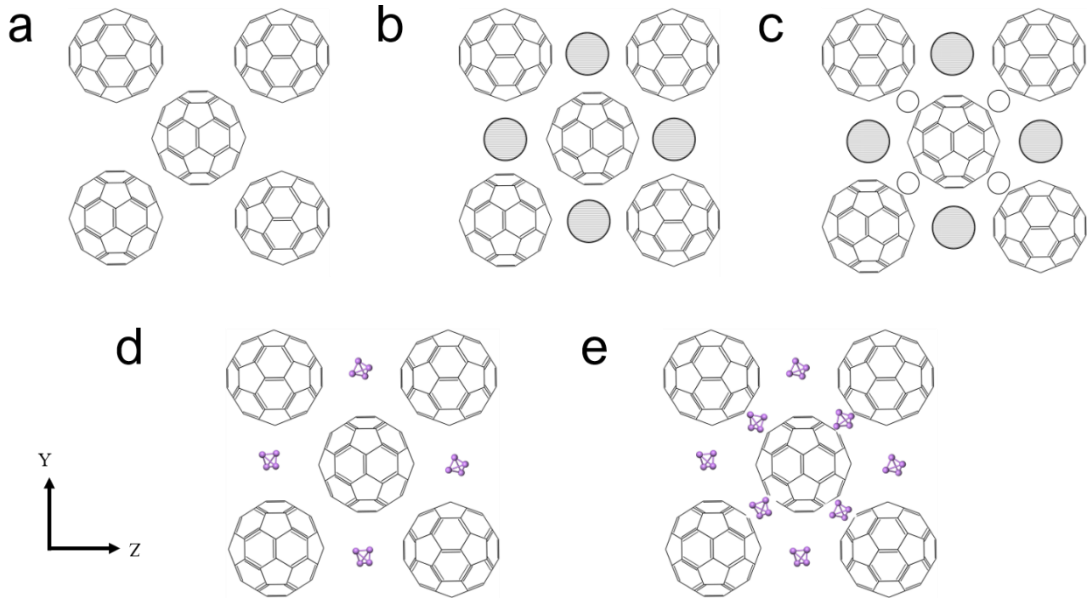

Figure. S2 The structure of (a) C_{60}, (b) Li_xC_{60} (x=1) and (c) Li_xC_{60} (x=3, 4) (d)Li_6C_{60} and (e) $Li_{12}C_{60}$. The big hatched and small open spheres are the octahedral sites and tetrahedral sites of the crystal, respectively. The purple atoms are lithium. **Related to Figure 3.**

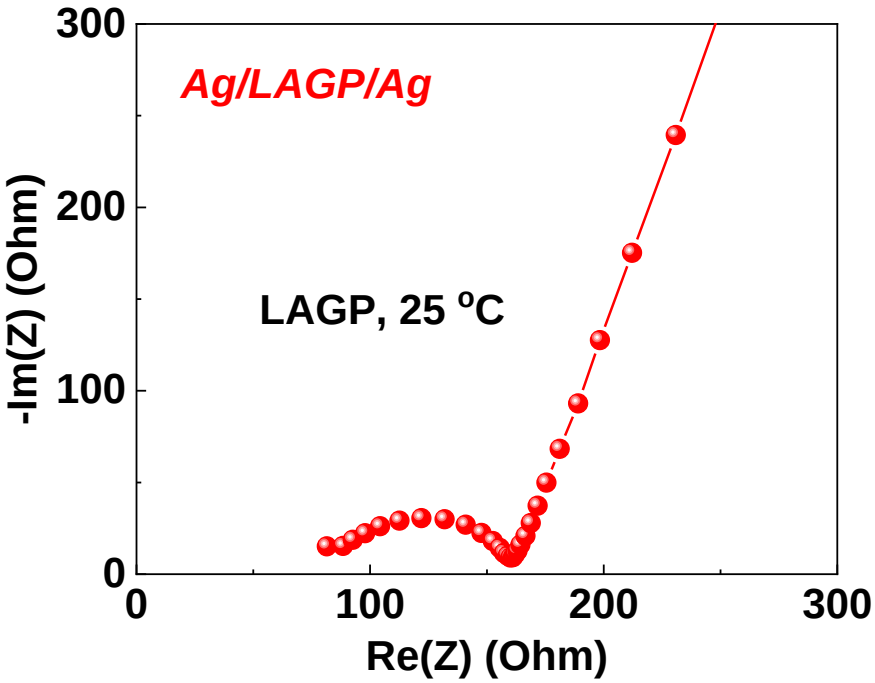

Figure. S3 The EIS plot of Ag/LAGP/Ag at 25 °C. The ionic conductivity of sintered LAGP pellet was calculated about 3.6×10^{-4} s cm^{-1}. The calculation was due to the equation u=b/(R S). u is the ionic conductivity; b is the thickness of the LAGP pellet; R is the impedence from EIS test; S is the cross-sectional area of LAGP pellet. **Related to Figure 3.**

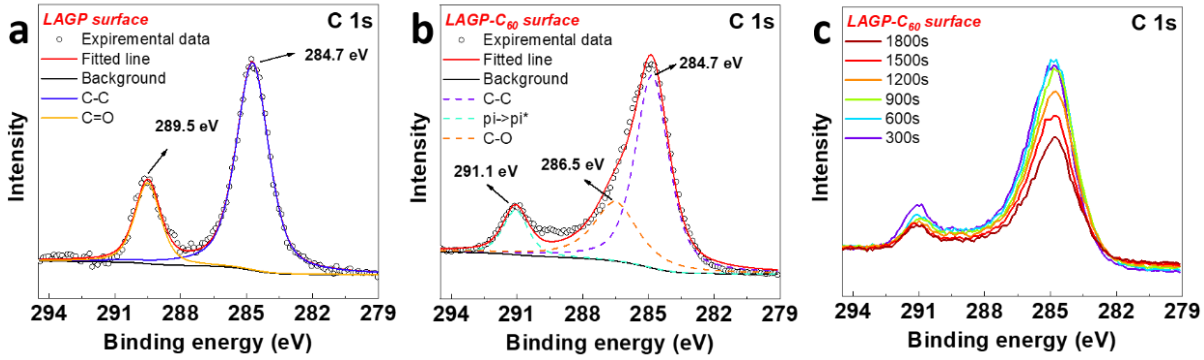

Figure. S4 C 1s XPS spectra of a) LAGP surface and b) LAGP-C_{60} surface with Ar^+ sputtering for 1800 s after 25 cycles. c) C 1s XPS spectra of LAGP-C_{60} surface with different sputtering time by Ar^+ after 25 cycles. **Related to Figure 6.**

Compared with the pristine LAGP, the C 1s XPS signal on the cycled LAGP surface presented a new peak at 289.5 eV, indicating that Li_2CO_3 was formed at the Li/LAGP interface after cycling, which is the product of the reaction between lithium metal and LAGP. This is

consistent with the previous work (Chung and Kang, 2017). Compared with the pristine LAGP-C_{60}, the C 1s XPS signal on the cycled LAGP-C_{60} surface presented two new peaks. One at 286.5 eV was due to the interaction of C_{60} with Li_2O on the surface of the lithium foil. The other at 291.1 eV was due to the interaction of C_{60} with lithium metal (Xu et al., 2020).

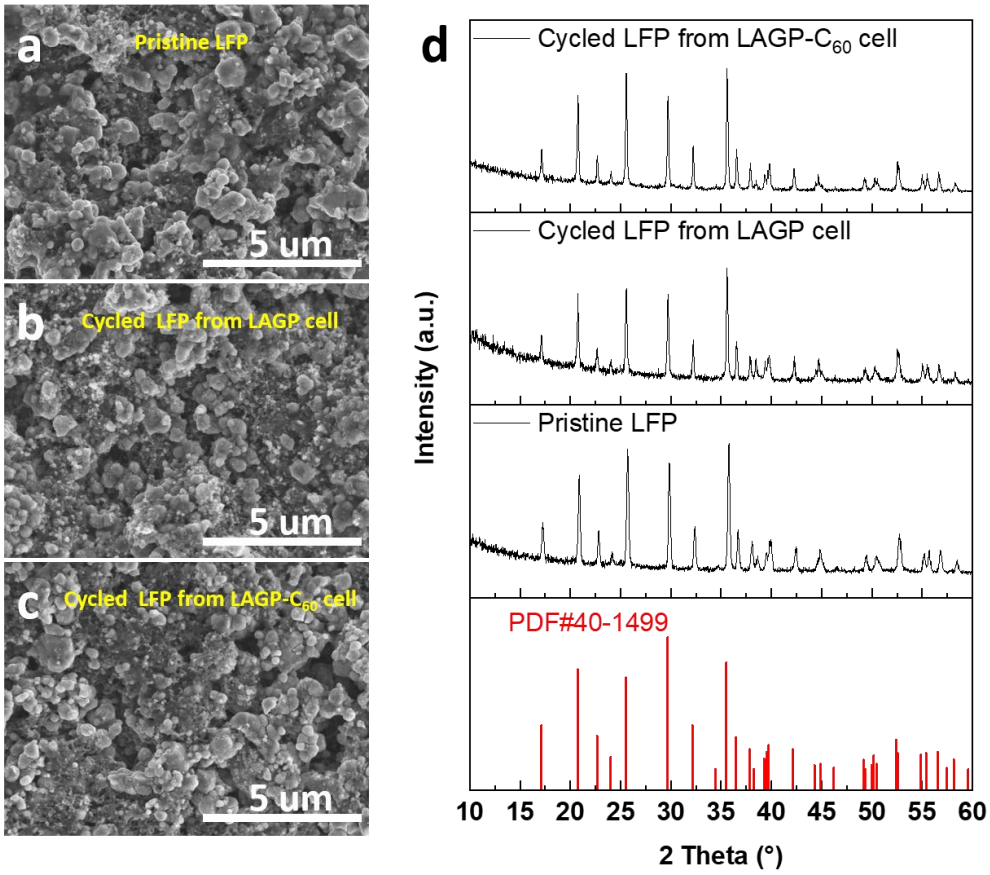

Figure S5 SEM images of a) pristine $LiFePO_4$ cathode, b) cycled $LiFePO_4$ cathode from Li/LAGP/$LiFePO_4$ cell and c) cycled $LiFePO_4$ cathode from Li/LAGP-C_{60}/$LiFePO_4$ cell. d) XRD pattern of cycled $LiFePO_4$ cathode from Li/LAGP-C_{60}/$LiFePO_4$, and Li/LAGP/$LiFePO_4$ cell, and pristine $LiFePO_4$ cathode. **Related to Figure 4.**

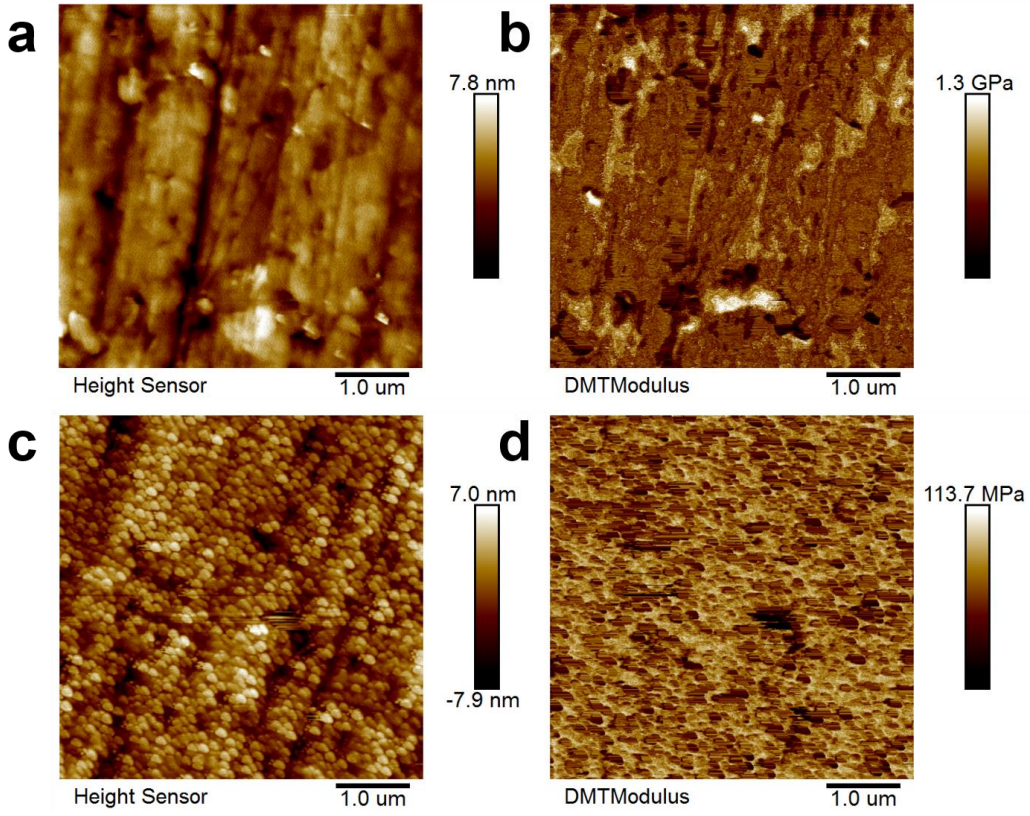

Figure S6. AFM height (a) and Young's modulus map (b) of LAGP surface. AFM height (c) and Young's modulus map (d) of LAGP-C_{60} surface. **Related to Figure 5.**

Supplemental References

Chung, H., and Kang, B. (2017). Mechanical and Thermal Failure Induced by Contact between a $Li_{1.5}Al_{0.5}Ge_{1.5}(PO_4)_3$ Solid Electrolyte and Li Metal in an All Solid-State Li Cell. Chem. Mater. *29*, 8611-8619.

Xu, Q., Lin, J., Ye, C., Jin, X., Ye, D., Lu, Y., Zhou, G., Qiu, Y., and Li, W. (2020). Air-Stable and Dendrite-Free Lithium Metal Anodes Enabled by a Hybrid Interphase of C_{60} and Mg. Adv. Energy Mater. *10*, 1903292.